CrystEngComm

PAPER

Evaporation-induced synthesis of carbon-supported Fe$_3$O$_4$ nanocomposites as anode material for lithium-ion batteries†

Yucheng Dong,[ab] Mingjun Hu,[b] Ruguang Ma,[b] Hua Cheng,[b] Shiliu Yang,[b] Yang Yang Li[b] and J. A. Zapien*[ab]

We report the high-yield preparation of carbon-supported superparamagnetic Fe$_3$O$_4$ nanocomposites (C–Fe$_3$O$_4$-NCs) using a simple evaporation-induced method. The Fe$_3$O$_4$ products consist of ~3–10 nm nanocrystals uniformly embedded in a carbon matrix to assemble nanoparticles with a size range from 40 to 80 nm. It is shown that lithium-ion batteries (LIB) assembled from heat-treated C–Fe$_3$O$_4$-NCs present attractive characteristics including a high specific capacity of 752 mA h g^{-1} at a current rate of 0.2 C for the second discharge cycle as well as good cycling performances with ~87% retained capacity after 100 cycles.

1 Introduction

Rechargeable LIBs are the most commercially utilized batteries for portable electronic devices such as mobile phones and digital cameras.[1,2] Rechargeable battery techniques have developed dramatically in the past decades, but their performance still lags behind the market demand; consequently, there is a strong need to search for new electrode materials with high specific capacities, low cost, good cycling performance, and high output. Recently, transition metal oxides have been widely investigated as anode materials for LIBs due to their high energy density and long cycling performance.[3–7] However, most transition metal oxides suffer from rapid capacity fading due to their intrinsically low electronic conductivity and large volume change during Li$^+$ insertion–extraction cycles.[8,9] Compared with other transition metal oxides such as Co$_3$O$_4$,[10] Mn$_3$O$_4$,[7] NiO,[11] RuO$_2$,[12] or SnO,[13] iron oxide nanocrystals (Fe$_3$O$_4$) are favorable due to low cost, high electronic conductivity and environmental benignity. As a result, Fe$_3$O$_4$ nanocrystals with distinguished magnetic and electrochemical properties have been widely used in various fields, such as information storage, drug delivery and targeting,[14,15] magnetic resonance imaging,[16] supercapacitors,[17,18] and rechargeable LIBs.[19–24] On the other hand, the superparamagnetic characteristics of Fe$_3$O$_4$ nanocrystals result in weak magnetic interaction between them and

thus effective reduced agglomeration in the absence of external fields. One of the main challenges of using transition metal oxides as anode materials is their poor cycling stability, which results from a large volume expansion occurring during cycling so that the electrodes cannot maintain their integrity over several discharge–charge cycles.

Coating nanocrystals with carbon is one of the most common methods to improve the cycling performance and capacity stability.[25–29] Significantly, a few reports are available on the fabrication of carbon coated iron oxide nanomaterials for LIBs applications[30–33] with enhancement of both the cycle and rate performance compared with bare or commercial iron oxides.[30] The carbon coating layer has an important role in enhancing the electronic conductivity of electrode materials, and serves as a protection barrier to effectively release the volume expansion of the inner active materials during the charge–discharge process. However, most methods for synthesizing such nanocomposites usually involve several time-consuming steps, such as centrifugation for product collection, rinsing with ethanol and water, and oven drying. It is therefore desirable to develop a high-yield and simple synthesis method to promote the applications of such functional nanocomposites.

Here, we report a high-yield and simple synthesis route to fabricate carbon-supported Fe$_3$O$_4$ nanocomposites for LIBs by heating DMF (*N*,*N*-dimethylformamide), Fe(acac)$_3$ (iron(III) acetylacetonate) and ascorbic acid (VC). In the reaction, VC serves as a carbon source, while DMF serves as a reductant to reduce part of Fe^{3+} to Fe^{2+}. The as-synthesized and heat-treated C–Fe$_3$O$_4$-NCs exhibit superparamagnetic behavior, which depends on the temperature of heat-treatment. We fabricated LIBs using the heat-treated C–Fe$_3$O$_4$-NCs, which exhibit a very high specific capacity of 752 mA h g^{-1} at a current rate of 0.2 C

*a*Center of Super-Diamond and Advanced Films, City University of Hong Kong, Hong Kong SAR, P. R. China. E-mail: apjazs@cityu.edu.hk
*b*Department of Physics and Materials Science, City University of Hong Kong, 83 Tat Chee Avenue, Kowloon, Hong Kong SAR, P. R. China

for the second discharge cycle and about 87% retained capacity after 100 cycles as well as a stable charge–discharge reversibility with Coulombic efficiency of ∼99% after the 14th cycle, thus indicating excellent cyclic stability.

2 Experimental section

2.1 Materials preparation

The C–Fe_3O_4-NCs were synthesized by a simple hydrothermal evaporation-induced method. In a typical synthesis, 3.53 g of iron(III) acetylacetonate ($Fe(acac)_3$; 97%, Aldrich) and 1.05 g of L-ascorbic acid (VC; reagent grade, Sigma) were dissolved in 10 ml of N,N-dimethylformamide (DMF; anhydrous, 99.8%, Sigma-Aldrich) under magnetic stirring for 10 min to give a red wine-colored solution. The resulting solution was transferred to a glass bottle (30 mL in volume), which was then heated to 180 °C in an electric oven for 5 h till the DMF solution evaporated completely. The sample was left to cool down naturally and the product was harvested from the glass bottle. The sample was then annealed in a tube furnace to 530 °C or 550 °C for 3 h under a continuous high-purity nitrogen gas to investigate the annealing effects such as improved carbonization degree and crystallinity. Bare Fe_3O_4 nanoparticles (see ESI† for details of the synthesis) were also prepared to compare its electrochemical performance.

2.2 Materials characterization

The as-prepared products were characterized using micro-area X-ray diffraction (XRD, Philips PW 1830 with Cu Kα radiation and a normal 2θ scan, 40 kV, 30 mA) with a 1 mm X-ray beam at room temperature. Fourier transform infrared (FTIR) spectra were recorded on a PE (Spotlight 3000) FTIR spectrometer using the KBr discs to investigate the different functional groups of as-synthesized and heat-treated C–Fe_3O_4-NCs. The weight ratio of KBr to as-prepared powders was 250 : 1, and 0.25 g of KBr was used in the preparation of the reference and sample discs. Raman measurements were employed to verify the chemical bonding characteristics of carbon with a Renishaw inVia Raman microscope using a laser line of 633 nm as the excitation source. To understand the approximate proportion of carbon in the synthesized products, thermal gravimetric analysis (TGA, Q50) was employed from room temperature to 800 °C under an air ventilation of 10 mL min^{-1} at a heating rate of 20 °C min^{-1}. The magnetic properties of the saturation magnetization (I_s) under a maximum applied field of 800 kA m^{-1} were measured with a vibrating sample magnetometer (VSM; 7410, Lake Shore, USA). The morphological characteristics of as-synthesized C–Fe_3O_4-NCs were investigated by utilizing scanning electron microscopy (SEM; Philips, XL 30FEG), transmission electron microscopy (TEM; Philips, CM20 operated at 200 kV), and high-resolution TEM (HRTEM; CM200 FEG operated at 200 kV).

2.3 Electrochemical performance evaluation

The electrochemical properties of the products were evaluated using coin cells (2032) assembled in an argon-filled glove box with Li metal foil (Aldrich, USA) as the counter electrode. The

anode slurry was prepared by mixing the active material, acetylene carbon black, and polyvinylidene fluoride (PVDF) binder (8 : 1 : 1 in a weight ration) in 1-methyl-2-pyrrolidinone (NMP) solvent. The working electrodes were prepared by coating a homogeneous slurry on a copper foil followed by drying at 120 °C for 10 h in vacuum, circular (1.6 cm^2) anode discs were then punched from the copper foil. The anode discs were weighed to determine the amount of active materials before assembled into coin-type cell. One layer of Celgard 2032 (Celgard, Inc., USA) served as the separator and $LiPF_6$ (1 mol L^{-1}) was dissolved in an ethylene carbonate (EC)–dimethyl carbonate (DMC) mixture (1 : 1 in a weight ration) as the electrolyte. Cyclic voltammograms (CVs) of the cells were measured on a CHI-660C electrochemical workstation at a scan rate of 0.1 mV s^{-1} in a potential range from 5 mV to 3.0 V at room temperature. Galvanostatic discharge–charge cycling measurement of the assembled cells was conducted in the voltage range from 5 mV to 3.0 V using different constant current densities on an Arbin Instruments (BT 2000, College Station, Texas, USA) battery cycler at room temperature. A CHI-660C electrochemical workstation was employed to perform electrochemical impedance spectroscopy (EIS) measurements over a frequency range of 10 MHz to 100 kHz with a potentiostatic signal amplitude of 5 mV.

3 Results and discussion

Fig. 1 shows the powder X-ray diffraction (XRD) patterns of the as-synthesized C–Fe_3O_4-NCs and heat treated samples using two different temperatures of 530 and 550 °C, under a continuous high-purity nitrogen gas flow. The diffraction peaks of both as-synthesized and 530 °C heat-treated nanocomposites, Fig. 1 curves (a) and (b), are in good agreement with the diffraction peaks of Fe_3O_4 (Magnetite, JCPDS 85-1436). As the heat-treatment temperature is
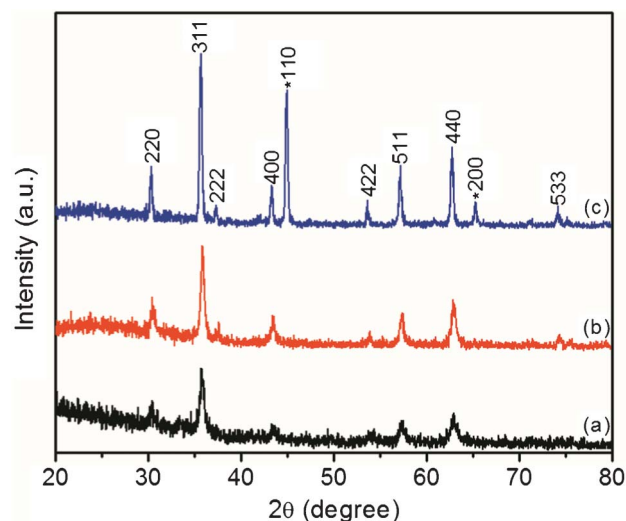

Fig. 1 XRD patterns of the C–Fe_3O_4-NCs (a) as-synthesized, and heat-treated at (b) 530 °C, and (c) 550 °C.

increased to 550 °C, iron Fe (iron, JCPDS 87-0721) appears besides Fe_3O_4 suggesting that Fe_3O_4 was partially reduced by carbon. Furthermore, all diffraction peaks become stronger and narrower indicating the recrystallization of Fe_3O_4 nanoparticles.

FTIR spectroscopy, Fig. 2, was employed to further investigate the structural change in bonding related to as-synthesized and heat-treated C–Fe_3O_4-NCs. In the case of the as-synthesized C–Fe_3O_4-NCs, the broad band at 3420 cm^{-1} is ascribed to the stretching vibration of O–H, arising from hydroxyl groups in the VC and possible water absorbed during the IR measurement. The bands at 2924 and 1420 cm^{-1} are assigned to stretching and bending vibrations of C–H bands, respectively, meanwhile the strong absorption bands at 1556 cm^{-1} can be attributed to the stretching vibration of C=C bonds.[34] The band at 1024 cm^{-1} arises from the stretching vibrations of C–N bonds, while the other absorptions around 660 cm^{-1} should be assigned to organic species. For heat-treated C–Fe_3O_4-NCs at 530 °C, the intense band in the spectra at 554 cm^{-1} is ascribed to the stretching vibration of Fe–O in Fe_3O_4.[35,36] The intensity of the band at 554 cm^{-1} decreased when heat-treated at 550 °C, Fig. 2(c), which may result from part of the Fe_3O_4 being reduced to elementary iron.

Fig. 3 presents the Raman spectra of the as-synthesized and C–Fe_3O_4-NCs heat-treated at 530 and 550 °C. The as-synthesized and heat-treated C–Fe_3O_4-NCs show a typical two-band Raman spectrum with the G band at 1594 cm^{-1} corresponding to an E_{2g} mode of graphite, namely, the stretching modes of C=C bonds of graphite, while the D band at around 1336 cm^{-1} is associated with the vibrations of carbon atoms with dangling bonds in plane terminations of disordered graphite or glassy carbon,[37] which confirmed the amorphous carbon structure.[38] The D/G intensity ratio of the three samples increased indicating the graphitization degree of carbon was improved with increasing annealing temperature.
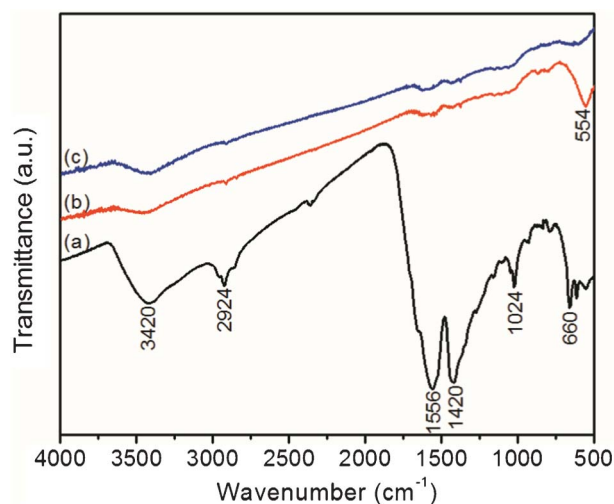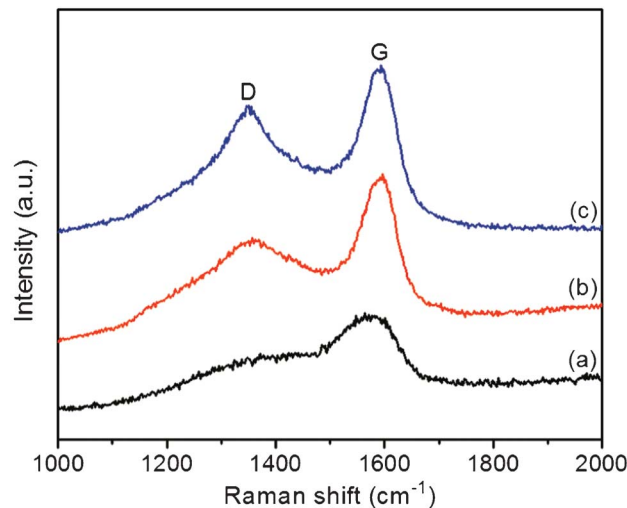

Fig. 3 Raman spectra of the C–Fe_3O_4-NCs (a) as-synthesized, and heat-treated at (b) 530 °C, and (c) 550 °C.

The carbon content in the 530 °C preheat treated sample was calculated based on the TGA curves, Fig. 4(a), assuming that the final residue is Fe_2O_3 resulting from the burning of the carbon and oxygenation of Fe_3O_4-related compounds under the continuous flow of O_2 gas at high temperatures. There is a slight weight gain at ∼260 °C, solid curve in Fig. 4(a), which corresponds to the oxidation of Fe_3O_4. As the temperature increases the combustion of carbon starts and is nearly completed at ∼620 °C. The approximate weight proportion of carbon, based on the curve and final residues, was evaluated to be 49.5%. By contrast, a noticeable region of weight gain can be observed in the TGA curve of Fig. 4(b) for the sample of heat-treated at 550 °C, which can be attributed to oxidation of the iron element and Fe_3O_4.

The as-synthesized C–Fe_3O_4-NCs nanoparticles are supported by carbon as shown by the SEM and TEM images in

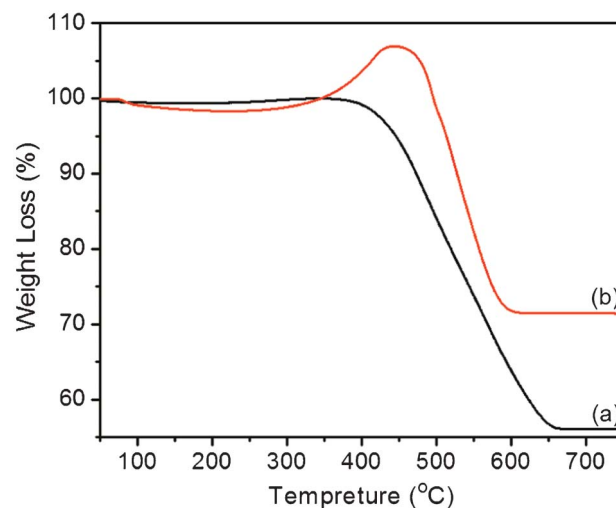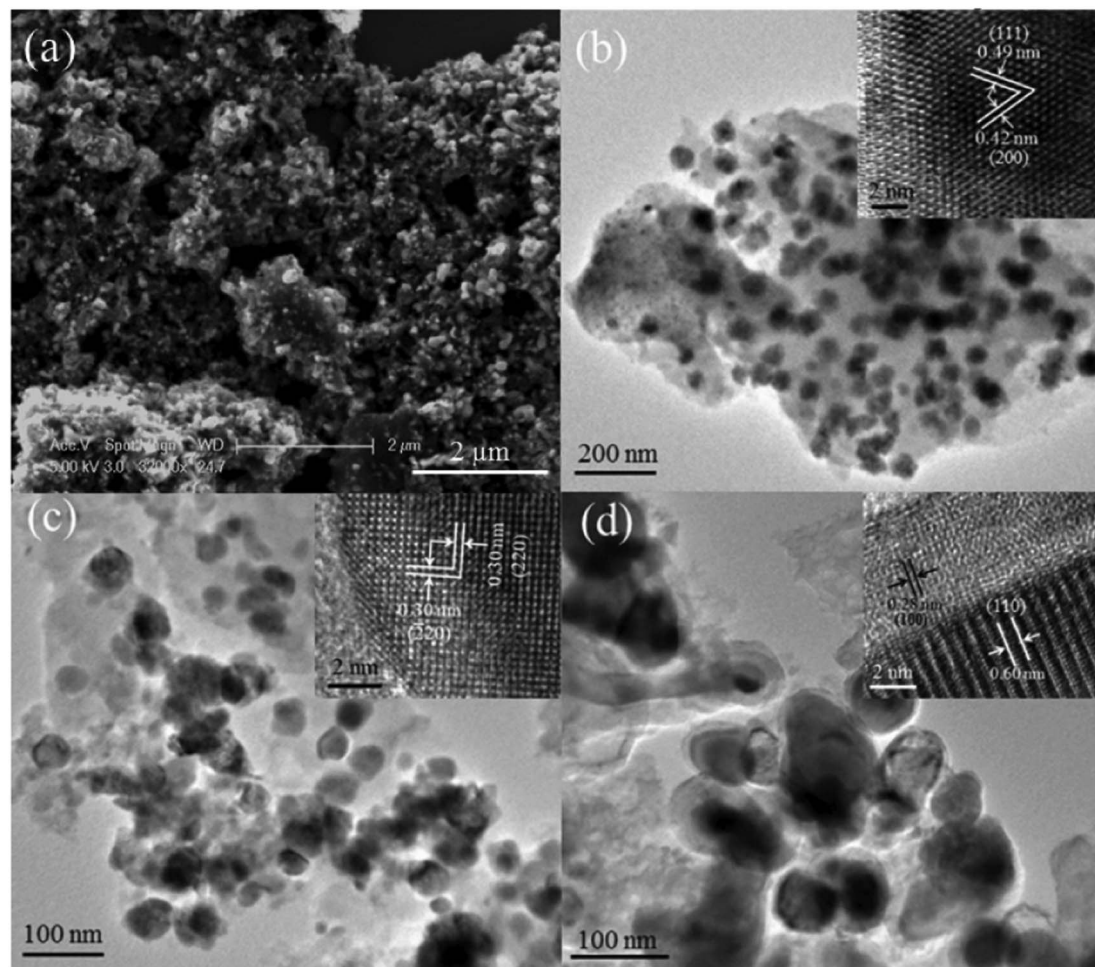**Fig. 2** FTIR spectra of the C–Fe_3O_4-NCs (a) as-synthesized, and heat-treated at (b) 530 °C, and (c) 550 °C.

Fig. 4 TGA curves of the C–Fe_3O_4-NCs heat-treated at (a) 530 °C and (b) 550 °C.

Fig. 5 SEM (a) and TEM (b) image of the as-synthesized C–Fe$_3$O$_4$-NCs; TEM image of the C–Fe$_3$O$_4$-NCs heat-treated at (c) 530 °C, and (d) 550 °C. The insets in (b)–(d) show HRTEM details of the edge of an individual nanoparticle.

Fig. 5(a) and (b), respectively. Furthermore, the TEM images of C–Fe$_3$O$_4$-NCs show that the size distribution of these particles is in the ∼40 to 80 nm in range, while smaller nanocrystals with sizes of ∼3–10 nm, which is in the superparamagnetic size range, can also be found dispersed in the supported carbon matrix as shown in Fig. S5 and S6 (see ESI† for detail). From the TEM and HRTEM results, we speculate that the big nanoparticles might be assembled by these small nanocrystals in the reaction process. The inset of Fig. 5(b) shows the HRTEM image of the edge of an individual Fe$_3$O$_4$ nanoparticle with lattice spacing of 0.42 and 0.49 nm, which is in good agreement with the *d*-spacing of the (200) and (111) planes, respectively. The condition of heat treatment plays an important role in adjusting the morphology of the products. Fig. 5(c) shows the TEM image of C–Fe$_3$O$_4$-NCs heat-treated at 530 °C, revealing that the size of these particles does not change significantly while their surface becomes smooth. The corresponding HRTEM image reveals the lattice spacing of 0.30 nm, which is consistent with the *d*-spacing of (220) and (220) planes observed in the inset of Fig. 5(c). When the heat-treatment temperature is increased to 550 °C, the size of the

primary nanoparticles becomes large and they aggregate severely, presumably because of phase transformation in the reduction process, as shown in Fig. 5(d). The corresponding HRTEM image, inset in Fig. 5(d), shows the edge of one such Fe$_3$O$_4$ nanoparticle with a lattice spacing of 0.60 nm, corresponding to the (110) plane. A thin layer of ∼5 nm thickness surrounding the Fe$_3$O$_4$ nanoparticle is observed with a lattice spacing of ∼0.28 nm, which can be ascribed to the (100) plane of metal iron, which is consistent with the XRD results and is thought to result from the Fe$_3$O$_4$ reduction by the carbon to iron when heat-treated at this temperature.

The hysteresis loops at room temperature (298 K) of the as-synthesized and heated-treated C–Fe$_3$O$_4$-NCs at different temperatures were measured by a vibrating sample magnetometer between −2 and 2 T, as shown in Fig. 6. Generally, the superparamagnetic phenomenon demands nanosized grains and a collection of single-domain particles that array as a large individual magnetic moment.[39] The *M–H* curve for the as-synthesized C–Fe$_3$O$_4$-NCs displayed in Fig. 6(a) show no measurable coercivity and remanence effect when the applied magnetic field was removed. These results and the magnetite
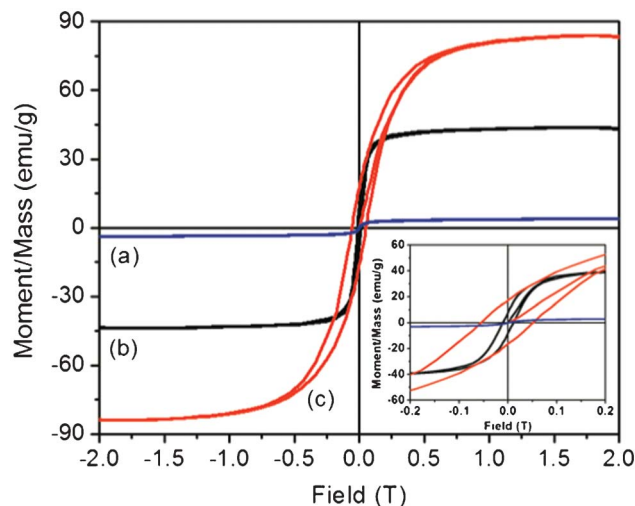
Fig. 6 Room-temperature hysteresis loops of the $C-Fe_3O_4$-NCs (a) as-synthesized, and heat-treated at (b) 530 °C, and (c) 550 °C. The inset shows the magnified version of the hysteresis loops.

Fig. 7 Cyclic voltammograms of the $C-Fe_3O_4$-NCs heat-treated at (a) 530 °C and (b) 550 °C from the first to the third cycle.

nanoparticles size in the superparamagnetic size range, as demonstrated by the TEM observations, Fig. 5, S5 and S6 in ESI† are a strong indication that the fabricated samples present superparamagnetic behavior. However, the as-synthesized $C-Fe_3O_4$-NCs exhibited a small saturation magnetization (M_s = 3.9 emu g^{-1}), which should be attributed to poor crystallinity of Fe_3O_4 at low temperature and the existence of a large proportion of organic residues. When the $C-Fe_3O_4$-NCs were heat treated at 530 and 550 °C, the value of the M_s increased to 43.7 and 83.5 emu g^{-1}, respectively; meanwhile, the coercivity (H_c) and retentivity (M_r) values increased as shown in Fig. 6(b) and (c). The obviously increased magnetic parameters were due to the removal of remanent elements and improved crystallinity of the nanoparticles. The higher magnetization of the heat-treated $C-Fe_3O_4$-NCs at 550 °C can be understood from the Fe_3O_4 nanoparticles partial reduction to iron element, inset in Fig. 5(d), with much larger saturation magnetization (M_s) compared to Fe_3O_4.

The electrochemical properties of the heat treated $C-Fe_3O_4$-NCs with respect to Li$^+$ insertion–extraction were also investigated. Cyclic voltammograms (CVs) analysis for the first three cycles in the voltage range from 5 mV to 3 V at a scan rate of 0.1 mV s^{-1} are shown in Fig. 7. The CV spectrum of the bare Fe_3O_4 nanoparticles is shown in Fig. S3 (see ESI†) for comparison. In Fig. 7, the peaks around 1.25 V in the first cathodic cycle can be assigned to the formation of $Li_xFe_3O_4$,[24] while the broad peaks around 0.68 V, could be attributed to the reduction of Fe^{3+} and Fe^{2+} to Fe^0 and to the irreversible reaction related to the decomposition of the electrolyte.[9] The first anodic peaks appeared at about 1.6 V and 1.45 V for the heat treated samples at 530 °C and 550 °C, Fig. 7(a) and (b), respectively, which correspond to the reversible oxidation of Fe^0 to Fe^{3+} and Fe^{2+}. The differences of the position and intensity of the reduction and oxidation peaks between the heat-treated $C-Fe_3O_4$-NCs and bare Fe_3O_4 nanoparticles might
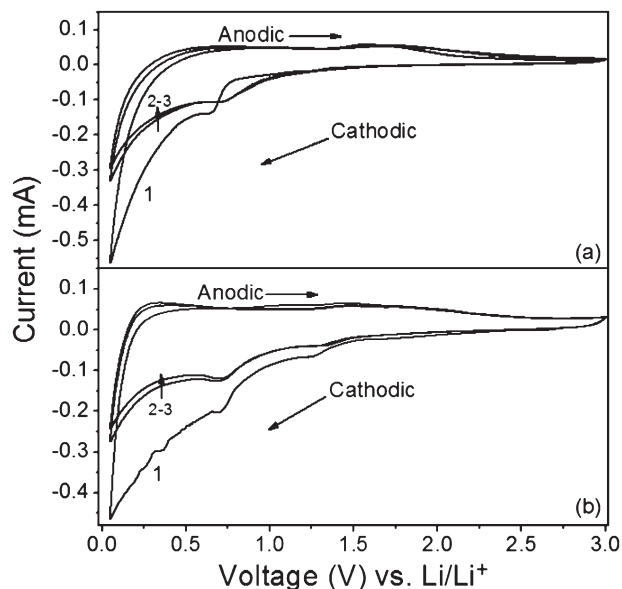
be ascribed to their distinct textural characteristics and particle sintering in heat treated samples.[40] In the following second and third cycles, both the cathodic and anodic peaks shift to the higher voltage ranges and the current of the peaks decreases revealing the existence of a certain degree of irreversibility of the redox reaction. However, there is no noticeable change for either cathodic or anodic peaks after the first cycle compared with the bare Fe_3O_4 nanoparticles (shown in Fig. S3, ESI†), suggesting the insertion–extraction of Li$^+$ ions taking place to the same extent, thus supporting our contention for good reversibility of the capacity of assembled batteries (see below). In addition, the cathodic peaks around 0.05 V and the anodic hump around 0.22 V can be ascribed to the lithiation and delithiation of the residual carbon component.

The theoretical capacities of carbon and Fe_3O_4 are 372 and 924 mA h g^{-1}, respectively, therefore, the heat-treated $C-Fe_3O_4$-NCs electrode has a theoretical capacity of 651 mA h g^{-1} calculated from the combination of carbon and Fe_3O_4.[41] The discharge–charge voltage profiles of $C-Fe_3O_4$-NCs heat-treated at 530 and 550 °C at a current density of 50 mA g^{-1} for the first cycle and 100 mA g^{-1} for the following four cycles are shown in Fig. 8(a) and (b), respectively. The first specific discharge capacities of the two samples are as high as 1653 and 1525 mA h g^{-1}, and the subsequent charge capacity can be retained at 965 and 733 mA h g^{-1}, corresponding to 58% and 48% of Coulombic efficiency, respectively. In contrast, the specific discharge–charge capacity of the bare Fe_3O_4, Fig. S3 in ESI† fades quickly showing poor cycling performance. It is noted that the initial discharge capacities of the three samples is much higher than the theoretical capacity of Fe_3O_4 (924 mA h g^{-1}), such higher-than-theoretical capacity values have been observed in the past for transition metal oxide anodes, which
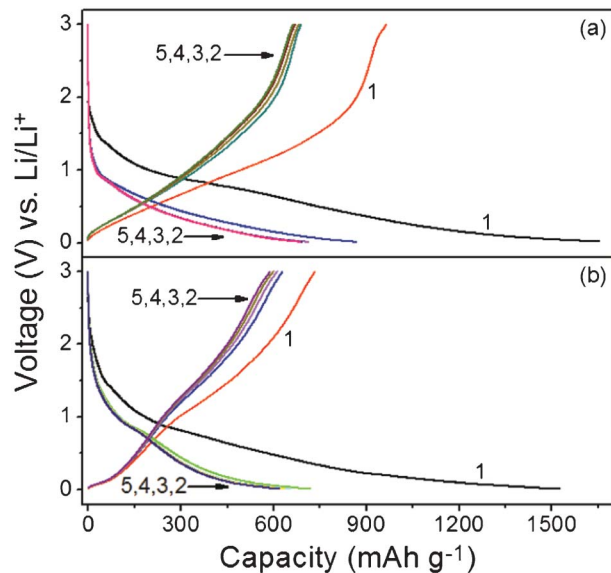
Fig. 8 Discharge–charge profile of the C–Fe$_3$O$_4$-NCs heat-treated at (a) 530 °C and (b) 550 °C at a current rate of 0.1 C.

could be attributed to the formation of a surface polymeric gel-like layer resulting from the decomposition of the electrolyte at low voltage in the first cycle that caused the high irreversible capacity.[9,42] After the second cycle, the capacity of the C–Fe$_3$O$_4$-NCs remains almost unchanged through the subsequent four discharge–charge cycles as shown in Fig. 8, but the heat treated sample at 530 °C presents much better electrochemical lithium performance.
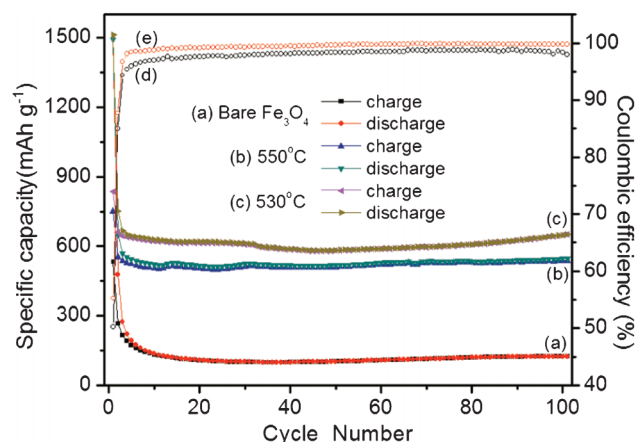
The heat-treated C–Fe$_3$O$_4$-NCs exhibit a much better rate performance compared to the bare Fe$_3$O$_4$ nanoparticles when operating at various rates between 0.1 and 1 C (considering 1000 mA g^{-1} as 1 C for simplicity) as shown in Fig. 9. All of the samples were first tested at a current rate of 0.05 C for the first cycle to activate the electrode materials while subsequent
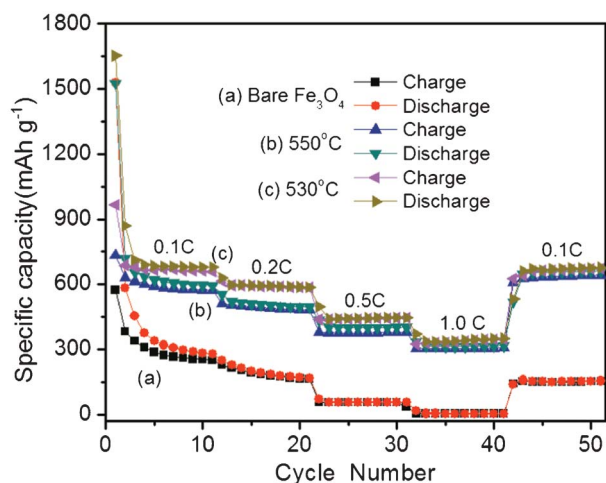
testing was performed for 10 cycles at each current rate. It is found that the observed capacities at each rate of the C–Fe$_3$O$_4$-NCs heat-treated at 530 °C were higher than those of samples heat-treated at 550 °C for the same current rate, which means that the heat-treatment temperature is crucial to the capacity of the C–Fe$_3$O$_4$-NCs fabricated by the evaporation-induced method. At high rates of 1 C, the specific discharge capacities of the C–Fe$_3$O$_4$-NCs heat-treated at 530 and 550 °C remain at 350 and 316 mA h g^{-1}, respectively, while the bare Fe$_3$O$_4$ nearly has no measurable capacity under this condition. More importantly, when the current rate was brought down to 0.1 C after such high current cycling, the discharge capacity of the electrode composed of the C–Fe$_3$O$_4$-NCs heat-treated at 530 and 550 °C swiftly recovered to 677 and 660 mA h g^{-1}, respectively, thus demonstrating excellent reversibility for the C–Fe$_3$O$_4$-NCs anode material.

Fig. 10 compares the cycling performance of the bare Fe$_3$O$_4$ and heat-treated C–Fe$_3$O$_4$-NCs electrodes for up to 100 cycles at the current rate of 0.2 C with a voltage window from 10 mV to 3 V. The capacity of bare Fe$_3$O$_4$ fades to 100 mA h g^{-1} after 20 cycles and then increases to 123 mA h g^{-1}. For the heat-treated sample at 530 and 550 °C, the discharge capacities drop gradually during the first 20 cycles to about 619 and 514 mA h g^{-1}, respectively, and remain almost constant between the 20th and 80th cycle, finally then increasing to 651 and 547 mA h g^{-1} until the 100th cycle as shown in Fig. 10(b) and (c), respectively, revealing their excellent cycle stability. The capacity of the sample heat-treated at 550 °C is lower than that of the sample heat-treated at 530 °C, which could be due to the decrease of the active materials caused by the reduction of part of the Fe$_3$O$_4$ to iron element by carbon. The capacity rise after prolonged cycling can be attributed to a possible activation process, in which the irreversible Li$_2$O formed during the early cycles could be re-exposed since the progressively pulverized particles resulted from electrochemical grinding effect thus participate in the electrochemical

Fig. 9 Rate capacity of (a) bare Fe$_3$O$_4$, and C–Fe$_3$O$_4$-NCs heat-treated at (b) 550 °C, and (c) 530 °C from 0.1 C to 1 C for 10 cycles at each current rate.

Fig. 10 The cycle performance of (a) bare Fe$_3$O$_4$ nanoparticles, and C–Fe$_3$O$_4$-NCs heat-treated at (b) 550 °C and (c) 530 °C and the corresponding Coulombic efficiencies of (d) 550 °C, and (e) 530 °C heat-treated C–Fe$_3$O$_4$-NCs at a current rate of 0.2 C.

reaction.[24,31] It can be found that the heat-treated C–Fe$_3$O$_4$-NCs electrodes show great enhancement of the capacities retention in comparison with the bare Fe$_3$O$_4$ nanoparticles electrode. The Coulombic efficiencies of the 530 and 550 °C heat-treated C–Fe$_3$O$_4$-NCs are illustrated in Fig. 10(c) and (d), respectively. It is noted that the Coulombic efficiency after the second cycle of the sample heat-treated at 530 °C is always higher than that of the sample heat-treated at 550 °C, suggesting a better charge–discharge reversibility of the 530 °C heat treated sample. For the sample heat-treated at 530 °C, the Coulombic efficiency is above 98% after the 3rd cycle, reaches 99% at the 14th cycle, and continues to increase up to 99.7% at the 100th cycle, indicating a high charge–discharge reversibility.

To verify the good performance of the heat-treated C–Fe$_3$O$_4$-NCs, ac impedance measurements were also conducted as shown in Fig. 11. From the Nyquist plots, it is obvious that the diameters of the semicircles for the electrodes composed of C–Fe$_3$O$_4$-NCs heat-treated at 530 and 550 °C in the high-medium frequency region are much smaller than those of the bare Fe$_3$O$_4$ electrode, which indicates that the charge-transfer resistances of the C–Fe$_3$O$_4$-NCs electrodes are smaller than that of the bare Fe$_3$O$_4$ electrode. This result demonstrated that the carbon layer serves as a conductive network, which improves the local conductivity, which leads to a high electrochemical performance for the heat-treated C–Fe$_3$O$_4$-NCs electrodes as anode materials for LIBs. In addition, the diameter of the 550 °C heat-treated electrode is smaller than that of 530 °C heat-treated electrode due to the existence of iron element, which decreases the charge-transfer resistance.

It is believed that the cycling and rate performances of the heat-treated C–Fe$_3$O$_4$-NCs improve due to the existence of carbon coating layers around the Fe$_3$O$_4$ nanoparticles. The supported carbon layer provides a better cushioning effect that prevents the volume expansion–contraction and aggregation of the possibly pulverized Fe$_3$O$_4$ nanoparticles during the subsequent charge–discharge process. Meanwhile, the heat-treated carbon layer can also improve the local conductivity, which is helpful for both the cycling and the rate performances,[8,24,30] thus supporting our contention that the presented high-yield and simple synthesis method of C–Fe$_3$O$_4$-NCs may have potential practical applications for the fabrication of lithium batteries.
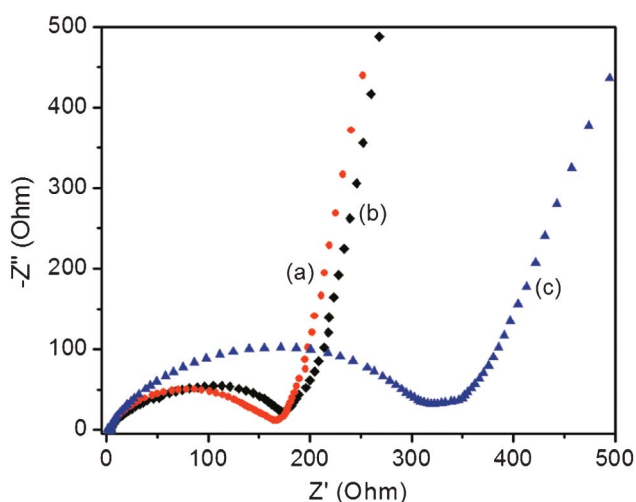
4 Conclusion

In summary, we synthesized C–Fe$_3$O$_4$-NCs using a facile high-yield and simple evaporation-induced synthesis route. The as-synthesized C–Fe$_3$O$_4$-NCs present superparamagnetic behavior at room temperature attributed to the presence of Fe$_3$O$_4$ nanocrystals (3–10 nm size range), which are present as a homogeneous distribution in carbon matrices and as building blocks for larger particles of 40–80 nm in size. The investigation of the electrochemical characteristics reveals that samples heat-treated at 530 °C show much better electrochemical properties with high reversible capacity, enhanced cycling performance, and excellent rate capability compared with those heat treated at 550 °C and the bare Fe$_3$O$_4$ nanoparticles electrodes. Furthermore, batteries assembled from 530 °C heat-treated C–Fe$_3$O$_4$-NCs electrodes exhibit a capacity of 752 mA h g^{-1} at a current rate of 0.1 C for the second discharge cycle, which is higher than the theoretical capacity of the C–Fe$_3$O$_4$-NCs. The heat treatment for the C–Fe$_3$O$_4$-NCs improves the crystallinity of Fe$_3$O$_4$ and removes organic residuals thus contributing to better electrochemical properties. However, the Fe$_3$O$_4$ nanoparticles are partly reduced to iron element for heat-treating temperatures higher than 530 °C. The improvement observed in the assembled LIBs can be ascribed to the synergistic effects between the Fe$_3$O$_4$ nanoparticles and carbon matrix, which serves as a buffer layer to prevent the volume change of the nanoparticles and as a conductive network to improve the local conductivity. These results demonstrate that the simple evaporation-induced high-yield synthesis method route to fabricate C–Fe$_3$O$_4$-NCs may have a promising application for anodic materials used in LIBs.

Acknowledgements

Fig. 11 Nyquist plot of the C–Fe$_3$O$_4$-NCs heat-treated at (a) 550 °C and (b) 530 °C, and (c) bare Fe$_3$O$_4$ electrodes.

Notes and references

1   M. Winter, J. O. Besenhard, M. E. Spahr and P. Novak, *Adv. Mater.*, 1998, **10**, 725.
2   M. S. Whittingham, *Chem. Rev.*, 2004, **104**, 4271.
3   P. Poizot, S. Laruelle, S. Grugeon, L. Dupont and J. M. Tarascon, *Nature*, 2000, **407**, 496.
4   S. Han, B. Jang, T. Kim, S. M. Oh and T. Hyeon, *Adv. Funct. Mater.*, 2005, **15**, 1845.

5   Y. M. Sun, X. L. Hu, W. Luo and Y. H. Huang, *ACS Nano*, 2011, **5**, 7100.

6   T. Muraliganth, A. V. Murugan and A. Manthiram, *Chem. Commun.*, 2009, 7360.

7   H. L. Wang, L. F. Cui, Y. Yang, H. S. Casalongue, J. T. Robinson, Y. Y. Liang, Y. Cui and H. J. Dai, *J. Am. Chem. Soc.*, 2010, **132**, 13978.

8   Y. G. Guo, Y. S. Hu, W. Sigle and J. Maier, *Adv. Mater.*, 2007, **19**, 2087.

9   Y. Z. Piao, H. S. Kim, Y.-E. Sung and T. Hyeon, *Chem. Commun.*, 2010, **46**, 118.

10   Z. S. Wu, W. C. Ren, L. Wen, L. B. Gao, J. P. Zhao, Z. P. Chen, G. M. Zhou, F. Li and H. M. Cheng, *ACS Nano*, 2010, **4**, 3187.

11   G. H. Yuan, Z. H. Jiang, A. Aramata and Y. Z. Gao, *Carbon*, 2005, **43**, 2913.

12   T. P. Gujar, V. R. Shinde, C. D. Lokhande, W. Y. Kim, K. D. Jung and O. S. Joo, *Electrochem. Commun.*, 2007, **9**, 504.

13   P. Meduri, C. Pendyala, V. Kumar, G. U. Sumanasekera and M. K. Sunkara, *Nano Lett.*, 2009, **9**, 612.

14   E. K. U. Larsen, T. Nielsen, T. Wittenborn, H. Birkedal, T. Vorup-Jensen, M. H. Jakobsen, L. Ostergaard, M. R. Horsman, F. Besenbacher, K. A. Howard and J. Kjems, *ACS Nano*, 2009, **3**, 1947.

15   X. Y. Yang, X. Y. Zhang, Y. F. Ma, Y. Huang, Y. S. Wang and Y. S. Chen, *J. Mater. Chem.*, 2009, **19**, 2710.

16   J. Salaklang, B. Steitz, A. Finka, C. P. O'Neil, M. Moniatte, A. J. van der Vlies, T. D. Giorgio, H. Hofmann, J. A. Hubbell and A. Petri-Fink, *Angew. Chem., Int. Ed.*, 2008, **47**, 7857.

17   J. Chen, K. L. Huang and S. Q. Liu, *Electrochim. Acta*, 2009, **55**, 1.

18   W. H. Shi, J. X. Zhu, D. H. Sim, Y. Y. Tay, Z. Y. Lu, X. Y. Zhang, Y. Sharm, M. Srinivasan, H. Zhang, H. H. Hnga and Q. Y. Yan, *J. Mater. Chem.*, 2011, **21**, 3422.

19   S. Mitra, P. Poizot, A. Finke and J. M. Tarascon, *Adv. Funct. Mater.*, 2006, **16**, 2281.

20   O. Delmer, P. Balaya, L. Kienle and J. Maier, *Adv. Mater.*, 2008, **20**, 501.

21   P. L. Taberna, S. Mitra, P. Poizot, P. Simon and J. M. Tarascon, *Nat. Mater.*, 2006, **5**, 567.

22   X. L. Wu, Y. G. Guo, L. J. Wan and C. W. Hu, *J. Phys. Chem. C*, 2008, **112**, 16824.

23   S. M. Yuan, Z. Zhou and G Li, *CrystEngComm*, 2011, **13**, 4709.

24   S. L. Jin, H. G. Deng, D. H. Long, X. J. Liu, L. Zhan, X. Y. Liang, W. M. Qiao and L. C. Ling, *J. Power Sources*, 2011, **196**, 3887.

25   X. L. Wu, L. Y. Jiang, F. F. Cao, Y. G. Guo and L. J. Wan, *Adv. Mater.*, 2009, **21**, 2710.

26   G. Derrien, J. Hassoun, S. Panero and B. Scrosati, *Adv. Mater.*, 2007, **19**, 2336.

27   J. Fan, T. Wang, C. Yu, B. Tu, Z. Jiang and D. Zhao, *Adv. Mater.*, 2004, **16**, 1432.

28   M. Noh, Y. Kwon, H. Lee, J. Cho, Y. Kim and M. G. Kim, *Chem. Mater.*, 2005, **17**, 1926.

29   A. L. M. Reddy, M. M. Shaijumon, S. R. Gowda and P. M. Ajayan, *Nano Lett.*, 2009, **9**, 1002.

30   W. M. Zhang, X. L. Wu, J. S. Hu, Y. G. Guo and L. J. Wan, *Adv. Funct. Mater.*, 2008, **18**, 3941.

31   T. Zhu, J. S. Chen and X. W. Lou, *J. Phys. Chem. C*, 2011, **115**, 9814.

32   L. Wang, Y. Yu, P. C. Chen, D. W. Zhang and C. H. Chen, *J. Power Sources*, 2008, **183**, 717.

33   J. S. Chen, Y. M. Zhang and X. W. Lou, *ACS Appl. Mater. Interfaces*, 2011, **3**, 3276.

34   B. J. Li, H. Q. Cao, J. Shao, M. Z. Qu and J. H. Warner, *J. Mater. Chem.*, 2011, **21**, 5069.

35   Y. Tian, B. B. Yu, X. Li and K. Li, *J. Mater. Chem.*, 2011, **21**, 2476.

36   G. Q. Xie, P. X. Xi, H. Y. Liu, F. J. Chen, L. Huang, Y. J. Shi, F. P. Hou, Z. Z. Zeng, C. W. Shao and J. Wang, *J. Mater. Chem.*, 2012, **22**, 1033.

37   Z. G. Lu, M. F. Lo and C. Y. Chung, *J. Phys. Chem. C*, 2008, **112**, 7069.

38   F. Tuinstra and J. L. Koenig, *J. Chem. Phys.*, 1970, **53**, 1126.

39   N. Z. Bao, L. M. Shen, Y. H. A. Wang, J. X. Ma, D. Mazumdar and A. Gupta, *J. Am. Chem. Soc.*, 2009, **131**, 12900.

40   D. Larcher, C. Masquelier, D. Bonnin, Y. Chabre, V. Masson, J. B. Leriche and J. M. Tarascon, *J. Electrochem. Soc.*, 2003, **150**, A133.

41   X. W. Lou, J. S. Chen, P. Chen and L. A. Archer, *Chem. Mater.*, 2009, **21**, 2868.

42   S. Laruelle, S. Grugeon, P. Poizot, M. Dolle, L. Dupont and J. M. Tarascon, *J. Electrochem. Soc.*, 2002, **149**, A627.